

MoO₂/C composites prepared by tartaric acid and glucose-assisted sol-gel processes as anode materials for Lithium-ion batteries

G.S. Zakharova^{1*}, L. Singer^{2*}, Z.A. Fattakhova¹, S. Wegener², E. Thauer², Q. Zhu³,
E.V. Shalaeva¹, R. Klingeler^{2,4}

¹*Institute of Solid State Chemistry, Ural Division, Russian Academy of Sciences, Yekaterinburg, Russia*

²*Kirchhoff Institute of Physics, Heidelberg University, Heidelberg, Germany*

³*Institute of Material Science and Engineering, Wuhan University of Technology, Wuhan, PR China*

⁴*Centre for Advanced Materials (CAM), Heidelberg University, Heidelberg, Germany*

*Both authors contributed equally.

Abstract

MoO₂/C-composites have been fabricated for the first time by a tartaric acid/glucose-assisted sol-gel method with post-annealing at 500 °C for 1 h in N₂ flow. The synthesized materials were fully characterized with respect to structure, morphology, and electrochemical properties. Compared with tartaric acid-assisted products, the adoption of glucose as carbon source effectively increases the carbon content in the composites. Irrespective of the organic component, the composites exhibit low crystallinity and small grain size. This results in good electrochemical performance of the anode materials as confirmed for the glucose-assisted materials which after additional post treatment delivers a competitive electrochemical capacity.

1. Introduction

Molybdenum dioxide (MoO_2), as an important semiconductor, has great potential applications in the production of chemical sensors [1], catalysts [2], field emission devices [3,4], and solar cells [5]. Additionally, MoO_2 has attracted considerable attention as electrode material for lithium ion batteries (LIB) because of its relatively large theoretical capacity (838 mA h g^{-1}) [6] and its high metallic conductivity ($6.04 \cdot 10^3 \text{ S cm}^{-1}$ for the individual rods) [7]. However, several of its intrinsic material properties limit the practical application of bulk MoO_2 , namely strong capacity fading and poor cycling stability originated by the huge volume changes during the charge/discharge processes as well as poor rate performance caused by the slow kinetics [8,11]. A variety of strategies have been employed to overcome this issue such as preparation of nanosized materials with different morphologies [9], doping with nitrogen [10], copper [11], and design of 3D hierarchically structures nanomaterials providing shorter lithium ion/electron diffusion distances and accommodating strain associated with strong volume changes upon cycling [12,13]. Additionally, incorporating MoO_2 with functional conductive carbonaceous materials like hollow carbon spheres [14], graphene [15], graphite oxide [16], is regarded as an effective strategy. A further way which advantageously yields homogeneous distribution of the carbon component, thereby increasing cycling stability of the materials is to introduce the carbonaceous phase during calcination of many different organic precursors such as aniline [17], dopamine [18,19], polyethylene glycol [20], alginate [21], ascorbic acid [22], glucose [23], or sucrose [24]. All functionalized materials display enhanced Li-retention performance in comparison with bulk MoO_2 , based on their higher surface areas, more active sites, shorter ion diffusion paths, and functioning carbon buffer which accommodate the strain.

Various techniques, such as a hydrothermal method [25,26], thermolysis [27], and electrospinning [28], have been developed to prepare composites based on MoO_2 . Herein, we present a new sol-gel synthesis approach to obtain MoO_2/C

composites. This method provides a molecular level-mixing of the starting materials and leads to better chemical homogeneity of the final products. Carbon coated MoO₂ particles have been produced by using glucose or tartaric acid as both reducing agents and carbon sources and the electrochemical performance of the resulting MoO₂/C composites as electrodes for Li-ion batteries was investigated.

2. Experimental

Molybdenum powder Mo (99.95% metal, Alfa Aesar), hydrogen peroxide H₂O₂ (30%, Merck), tartaric acid C₄H₆O₆ (AppliChem), and glucose C₆H₁₂O₆ (Sigma-Aldrich) were utilized for the synthesis. Firstly, 1.0 g of Mo powder was dissolved in 35 ml H₂O₂ at 10-15 °C to form a clear yellow solution of peroxomolybdic acid. Secondly, tartaric acid was dissolved in distilled water and stirred for 10 min. The molar ratio of tartaric acid to molybdenum metal was 1 : 1. Then, the solution of tartaric acid was slowly added into the solution of peroxomolybdic acid. To get a gel, the solution was heated at 60 °C under continuous stirring. The resulting gel was dried at 60 °C in air and calcinated at 500 °C for 1 h in N₂ flow to yield the MoO₂/C composite. At lower annealing temperatures, the materials were amorphous while annealing at 500 °C yields crystalline samples. The as-prepared product is labeled as MoO₂/C-T. For comparison, MoO₂/C was produced in a glucose-assisted process at a molar ratio of Mo : glucose = 1 : 1 and denoted as MoO₂/C-G. To study the effect of pounding on the electrochemical activity, MoO₂/C-G powder was colloiddally grinded (300 Us⁻¹) in ethanol using Ø 1mm ZrO₂ balls in a PM 100 planetary mill (Retsch) for 6 h, later annealed¹ at 500 °C for 1 h in N₂ and afterwards hand grinded in a mortar for 15 min; this sample is labeled as MoO₂/C-G(M).

X-ray diffraction (XRD) patterns were obtained on a Bruker AXS D8 Advance Eco using Cu K α radiation with a step size of $\Delta 2\theta = 0.02^\circ$. The morphology of the powder was determined by a ZEISS Leo 1530 and a JEOL

JSM-7610F scanning electron microscope (SEM), a JEOL JEM 2100 and a JEMe200 CX transmission electron microscope (TEM), respectively. In order to monitor the microstructural changes of MoO₂ upon cycling, ex-situ SEM studies were performed using a JEOL JSM-7610F scanning electron microscope. The cycled electrodes were disassembled in an Argon glove box, washed with ethylene carbonate and then dried overnight.

Fourier transform infrared (FT-IR) spectra were recorded using Spectrum One B (Perkin-Elmer) with an automatic diffuse reflectance accessory. A thoroughly ground sample was applied as a thin layer to a purpose-designed holder plate. Thermogravimetric analysis (TG-DSC-MS) with a heating rate of 10 K·min⁻¹ starting from room temperature up to 750 °C under flowing air was carried out using STA 449 F₃ Jupiter thermoanalyzer (Netzsch) coupled with a QMS 403 mass spectrometer. Raman spectra were measured with a Renishaw U1000 spectrometer at a laser wavelength of 532 nm.

Electrochemical measurements were carried out in Swagelok-type cells (see [29]). Working electrodes were prepared by mixing the active material, carbon black and polyvinylidene fluoride (PVDF) in N-methyl-2-pyrrolidinone (NMP) and stirred for 24 h before the resulting slurry was pasted on copper net current collectors. The as-prepared electrodes were dried in a vacuum oven (80 °C, 10 mbar) overnight, pressed and dried again. Fiberglass (Whatman GF/D) was used as separator and pure lithium metal foil (Aldrich) as counter electrode. The electrolyte was 1 M LiPF₆ in a mixture of ethylene carbonate and diethylcarbonate (1 : 1 by weight). Cell assembly was carried out in an Ar-filled glovebox with controlled moisture and oxygen concentration. Cyclic voltammetry (CV) at a scan rate of 0.1 mV s⁻¹ and galvanostatic cycling with potential limitation (GCPL) at specific currents of 100 mA g⁻¹, both in the voltage range of 0.01 - 3.0 V vs. Li/Li⁺, were carried out on a VMP3 potentiostat (BioLogic) at 25 °C.

3. Results and discussion

Fig. 1 shows X-ray diffractograms of the synthesized materials, i.e., MoO₂/C-G, MoO₂/C-G(M), and MoO₂/C-T. All observed peaks correspond to monoclinic MoO₂ and are accordingly indexed in a monoclinic lattice system with space group P2₁/c. The post treatment of the as-prepared composite does not change its structure. The experimentally determined lattice parameters of MoO₂ in the composite MoO₂/C materials are in a good agreement with theoretical values from JCS D no. 72-4534 (cf. Table 1).

Table 1. Experimentally determined lattice parameters of MoO₂ in MoO₂/C-G, MoO₂/C-G(M), and MoO₂/C-T as well as values from JCS D no. 72-4534.

	<i>a</i> (Å)	<i>b</i> (Å)	<i>c</i> (Å)	<i>β</i> (deg.)	<i>V</i> (Å ³)
MoO ₂ /C-G	5.652(6)	4.832(5)	5.594(7)	120.39(6)	131.7(3)
MoO ₂ /C-G(M)	5.679(5)	4.808(9)	5.619(8)	120.48(2)	132.2(3)
MoO ₂ /C-T	5.648(3)	4.912(6)	5.609(1)	119.24(7)	135.8(2)
MoO ₂	5.6109	4.8562	5.6285	120.95	131.53

The XRD data exhibit broad diffraction peaks with rather weak intensity which suggests that MoO₂ formed in the composites displays poor crystallinity and small crystal size. The mean primary crystallite size of the as-synthesized samples can be estimated using Scherrer's equation [30]:

$$D = K\lambda/\Delta(2\theta)\cos\theta, \quad (1)$$

where *D* is the average grain size based on the particular reflecting crystal face (hkl) direction, *K* is a shape factor which can be approximated to 0.9, *λ* is the wavelength of the applied Cu K α radiation, $\Delta(2\theta)$ is the full width at half-

maximum of the diffraction peak, and θ is the Bragg angle. Analysis² of the (011), (200), and (022) peaks yield to a mean primary crystallite size of around 6 nm for MoO₂/C-G, MoO₂/C-G(M), and MoO₂/C-T composites under study. The crystal structure of monoclinic MoO₂ is depicted in Fig. 1. It consists of MoO₆ octahedrons which form channels along the *a*-axis which are supposed to facilitate Li⁺ transport during electrochemical cycling.

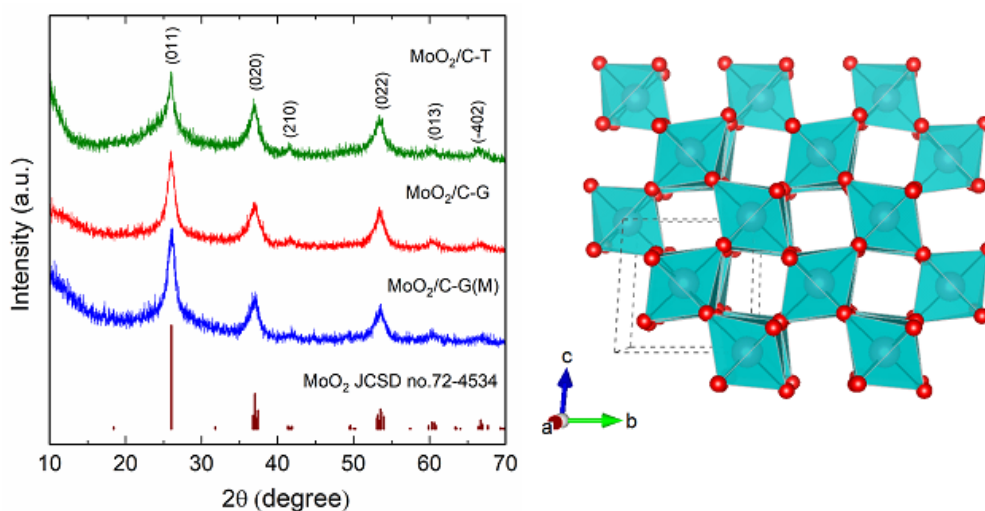


Fig. 1. XRD patterns of the MoO₂/C-G and the MoO₂/C-T composites (left), and a schematic of the corresponding crystal structure of MoO₂ (right).

Scanning electron microscopy images in Fig. 2 show the morphology of the as-prepared composites. Both as-prepared composite materials MoO₂/C-T and -G consist of irregular micro-sized agglomerates (Fig. 2a, c). The underlying primary particles, which are well visible in the high-magnification SEM images in Fig. 2b and d, in both composites consist of round grains with an average particle size of less than 20 nm. A further post treatment of the sample results in a visible size reduction of the agglomerates (Fig. 2e-f).

² Additional contributions to peak broadening are neglected.

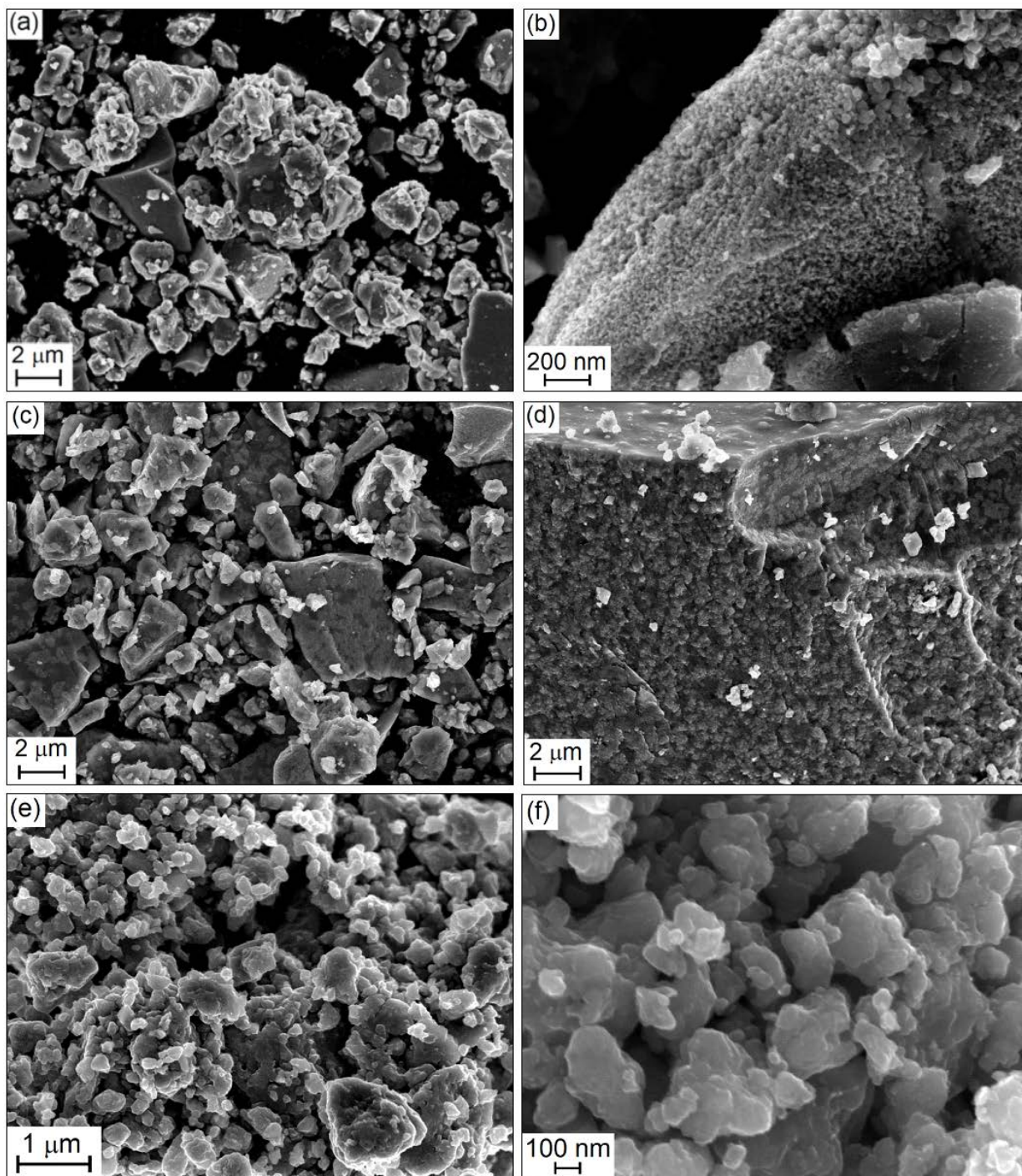


Fig. 2. SEM and high-magnification SEM images of (a, b) MoO₂/C-T, (c, d) MoO₂/C-G, and (e, f) MoO₂/C-G(M) obtained by a post treatment (see the text).

Additional detailed information on MoO₂/C-G is obtained from the TEM images in Fig. 3a. The images show the presence of MoO₂/C-G nanocrystallites forming large agglomerates that are dispersed in an amorphous carbon matrix.

Lattice fringes visible in the high-resolution TEM (HR-TEM) image (Fig. 3b) indicate lattice display spacings of approximately 0.35 nm. This value corresponds well with the (011) plane of MoO₂ which according to our XRD analysis has a plane distance of 0.3417(3) nm in MoO₂/C-G. Fig. 3b also shows carbon layers of around 10 nm in thickness around the crystallites. Selected area electron diffraction (SAED) confirms the crystalline structure of MoO₂ in the MoO₂/C-G nanocomposite (Fig. 3c). Debye rings from the SAED pattern demonstrate the ultrafine structure of crystalline MoO₂ without any preferred orientation of the individual crystallites. The Debye rings can be attributed to the monoclinic phase of MoO₂ with P2₁/c space group symmetry, which agrees with the XRD results.

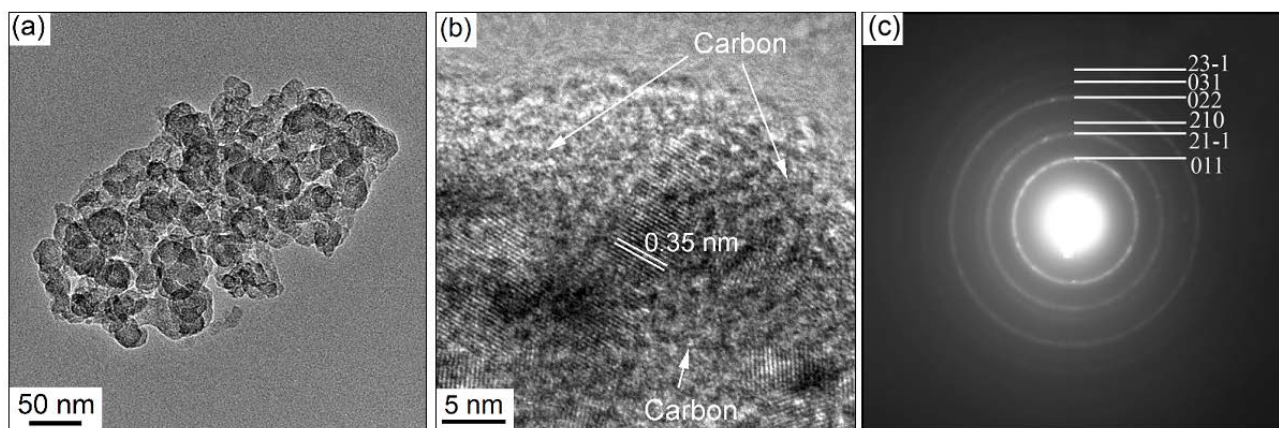


Fig. 3. (a) TEM image, (b) HRTEM image, and (c) SAED pattern of MoO₂/C-G composite.

Raman spectra of the MoO₂/C composites shown in Fig. 4a provide information on both the MoO₂ and the carbon components of the nanocomposite as the observed Raman peaks refer to Mo-O as well as carbon modes. The prominent carbon modes are the G-band which corresponds to the sp²-bonded carbon atoms and the D-band associated with defects or disorder mainly due to sp³-hybridization of carbon atoms [31]. The D- and G-bands of MoO₂/C-G composite arise at 1372 cm⁻¹ and 1586 cm⁻¹, respectively. In comparison, the G- and D-bands of MoO₂/C-T are at slightly lower wavenumbers of 1365 and 1575 cm⁻¹. The ratio of the

maximum intensities of these peaks, I_D/I_G , was calculated as 0.78 and 0.71 for MoO₂/C-G and MoO₂/C-T composites, respectively. This indicates that in comparison with tartaric acid, glucose promotes the formation of defects and disorder in the carbon component of the composite. In comparison with the pure MoO₂ phase [32], a richer Raman spectrum of MoO₂/C composites with intensive bands below 1000 cm⁻¹ resulting from different vibration modes of Mo-O is observed. The presence of the peaks located at 819 and 993 cm⁻¹ corresponding to the stretching vibrations of Mo=O bonds indicates the formation of the layered structure of the compounds similar to MoO₃ [33]. This phenomenon has been reported by Camacho-Lopez *et al.* [34] who associated it with the oxidation of MoO₂ to MoO_{2+δ} by laser irradiation.

FT-IR spectra of the MoO₂/C composites are shown in Fig. 4b. There are two typical vibration modes belonging to the MoO₂ phase [35]. The stretching vibrations of Mo=O bonds are demonstrated by the characteristic bands at 957 and 955 cm⁻¹ for MoO₂/C-T and MoO₂/C-G composites, respectively. The bridge stretching vibration of Mo-O-Mo bonds are displayed by the bands at 718 and 693 cm⁻¹ for MoO₂/C-T and MoO₂/C-G composites, respectively. The peaks at 1598 cm⁻¹ (MoO₂/C-T) and 1600 cm⁻¹ (MoO₂/C-G) are assigned to the C-O stretching vibration in the carboxylic group which may result from incomplete decomposition of the organic groups in the carbon component. The weak bands located at around 3400 cm⁻¹ and 1640 cm⁻¹ are associated with the stretching and bending vibrations of O-H, respectively, originating from trace amounts of adsorbed water in the powder. It is worth noting that the peaks which are attributed to pure glucose [36] and tartaric acid [37] are not part of the respective spectra.

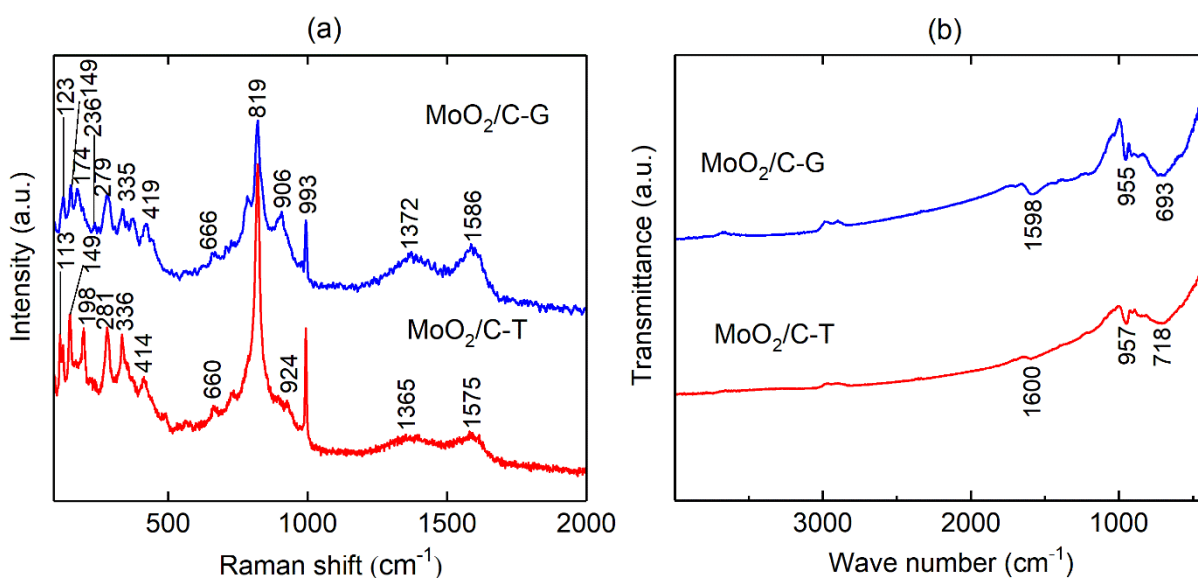


Fig. 4. (a) Raman and (b) FT-IR spectra of $\text{MoO}_2/\text{C-G}$ and $\text{MoO}_2/\text{C-T}$ composites.

In order to determine the thermal stability of MoO_2/C composites in air and to quantify the amount of carbon within the materials, TG-DSC-MS studies of as-prepared materials were carried out (Fig. 5). The TG curve of the $\text{MoO}_2/\text{C-G}$ composite evidences two steps of weight loss (Fig. 5a). We attribute the first weight loss of 5.7 wt% in the temperature regime from 70 °C to 300 °C mainly to evaporation of water. It appears as a weak and broad endothermic process centered at 115 °C. The second weight loss of 23.7 wt% from 300 °C to 690 °C is caused by oxidation of carbon components and the release of CO_2 gases. The mass spectrometry curve (ion current versus temperature) indicates that the main gaseous product of $\text{MoO}_2/\text{C-G}$ decomposition is CO_2 ($m/z = 44$ a.e.m.). However, the carbon component of $\text{MoO}_2/\text{C-G}$ was not completely oxidized to CO_2 at 690 °C. Despite the appearance of a two-step process somehow similar to what is observed in $\text{MoO}_2/\text{C-G}$, the TG curve of $\text{MoO}_2/\text{C-T}$ shown in Fig. 5b shows several differences. Again, a first stage from 25 to 300 °C with corresponding weight loss of 3.6 wt% can be assigned to evaporation of surface-adsorbed water. The second region of mass loss (2.4 wt%) from 300 to 514 °C is accompanied by a broad exothermic peak. It is attributed to the decomposition and full oxidation of organics. From the mass spectrometry curve, it can be revealed that the main

gaseous product of $\text{MoO}_2/\text{C-T}$ decomposition is CO_2 ($m/z = 44$ a.e.m.). Additionally, the three steps observed in TGA suggest that the carbon component in the $\text{MoO}_2/\text{C-T}$ composite has three states differently bound to the main phase (MoO_2). At around 550°C , the TG data indicate an increase of sample weight by 2.9 wt%. This process is attributed to the oxidation of Mo^{4+} to Mo^{6+} and results in the formation of MoO_3 as a final thermolysis product. Based on the assumptions made above, the calculated carbon contents in $\text{MoO}_2/\text{C-T}$ and $\text{MoO}_2/\text{C-G}$ composites are 2.4 and more than 23.7 wt%, respectively.

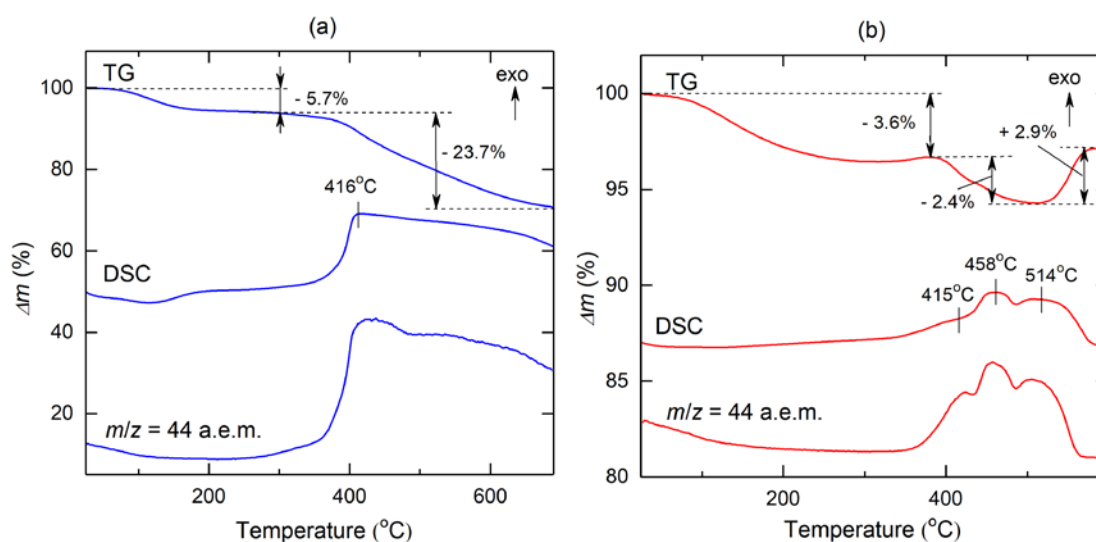


Fig. 5. Thermogravimetry, DSC, and mass spectroscopy curves of (a) $\text{MoO}_2/\text{C-G}$ and (b) $\text{MoO}_2/\text{C-T}$ composites.

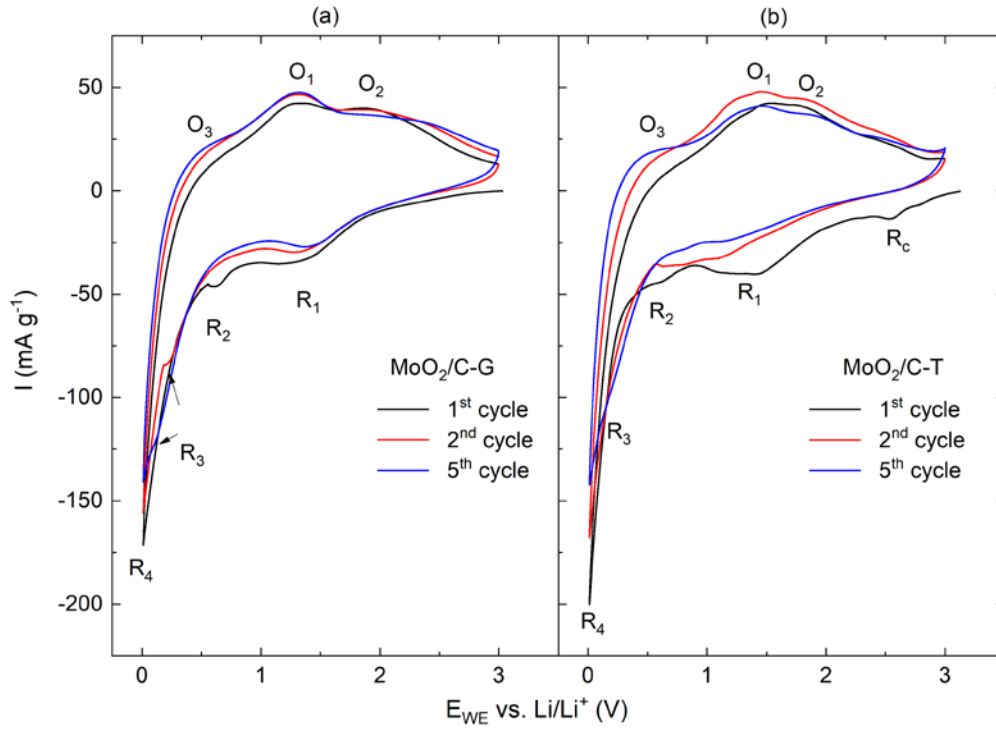
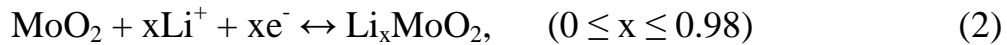


Fig. 6. Cyclic voltammograms of (a) MoO₂/C-G and (b) MoO₂/C-T composites recorded at a scan rate of 0.1 mV s⁻¹.

The electrochemical properties of the composite materials obtained as described are investigated with respect to their applicability as electrode materials in LIB by means of CV and GCPL. Fig. 6 displays the first, second, fifth CV curve of MoO₂/C-G and MoO₂/C-T. The reversible reactions of MoO₂ with lithium are described by the following electrochemical reactions [16,38]:



Due to the deliberate low crystallinity of the samples, mainly extended areas of electrochemical activity instead of well-defined peaks are visible in the CV. In the first reductive sweep of MoO₂/C-G, four different cathodic features are observed. The elevation at around 1.25 V (R1) can be attributed to the phase transition between the orthorhombic and the monoclinic phase upon lithium insertion (Eq. 2) as suggested by Dahn et al. [39]. Due to the absence of the peak R2 at around 0.6 V in further cycles, it is most likely assigned to the solid electrolyte interface (SEI)

formation which is consistent with reports by Luo *et al.* [40] and Xu *et al.* [41]. The reversible conversion reaction (Eq. 3) can be assigned to the reduction peak R3, parts of R4 and the elevation O3 [38]. The two overlapping oxidation peaks O2 and O1 can be ascribed to the phase transitions (monoclinic-orthorhombic-monoclinic) in partially lithiated Li_xMoO_2 [42]. The main difference between the CV of $\text{MoO}_2/\text{C-G}$ (Fig. 6a) and $\text{MoO}_2/\text{C-T}$ (Fig. 6b) is the presence of the feature Rc at around 2.5V in the first reductive sweep of the latter. In the literature, Rc is sometimes observed [27,43] and sometimes not [42,44] and its origin is yet unclear.

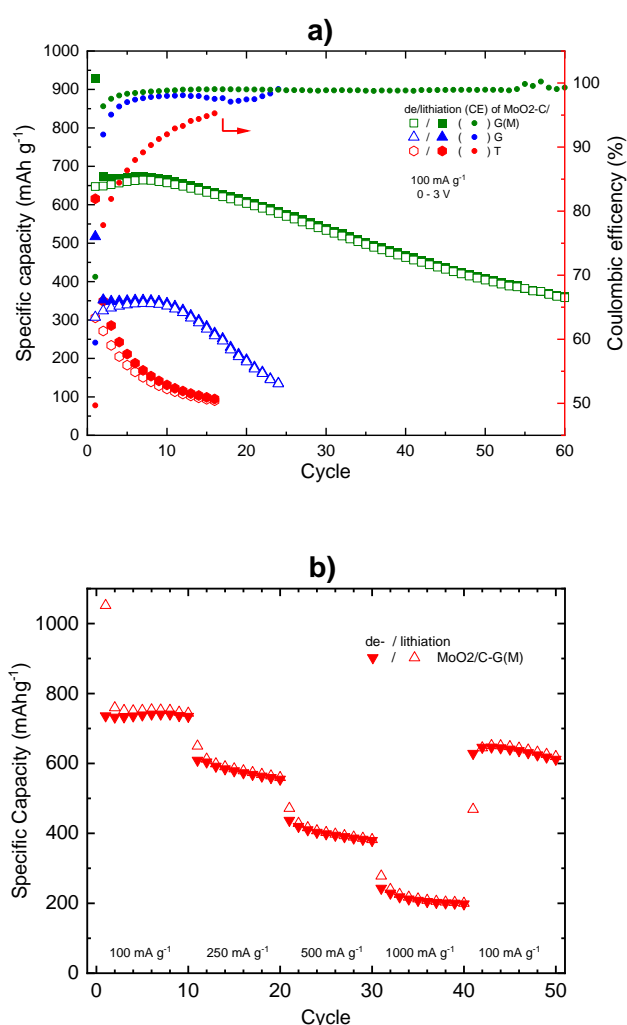


Fig. 7 a) Specific charge/discharge capacities and associated coulombic efficiencies of MoO_2/C electrodes and b) rate capability test with different cycling rates of $\text{MoO}_2/\text{C-G(M)}$ electrode measured by GCPL between 0.01 V and 3 V.

The cycling performance of as-prepared MoO₂/C-G- and MoO₂/C-T- as well as of MoO₂/C-G(M)-based electrodes is presented in Fig. 7a. The corresponding potential profiles are shown in Fig. S1-S3. The electrochemical performance of the MoO₂/C composites show strong differences. The highest discharge capacity in the first and twentieth cycle of 928 mAh g⁻¹ and 610 mAh g⁻¹ is reached by the post treated sample MoO₂/C-G(M). In contrast, the as-prepared material MoO₂/C-G achieves 516/195 mAh g⁻¹, respectively. Coulombic efficiencies also shown in Fig. 7a confirm significant irreversible effects not only for MoO₂/C-T but also for MoO₂/C-G. All materials display reduced Coulombic efficiency in the first cycles which is attributed to common irreversible processes as electrolyte decomposition and formation of the SEI [22,40,41]. Similarly to what is concluded from the evolution of capacity upon cycling, Coulombic efficiencies for MoO₂/C-G(M) are highest and amount to about 98 %. MoO₂/C-T has in comparison to MoO₂/C-G a high initial discharge capacity of 617 mAh g⁻¹ but shows a much severe drop in capacity already in the second cycle. We attribute this to the much lower (i.e., by more than 20%) carbon content. Such a low carbon content may result in an increased contact loss between the active material and the current collector during cycling. This degeneration process is well known for conversion-type materials and occurs due to the volume expansion and the associated induced pulverization during the conversion reaction [45–47]. Comparison of the treated and untreated MoO₂/C-G samples shows that the post treated sample MoO₂/C-G(M), which features a reduced size of the agglomerates (Fig. 2e-f), achieves nearly 2 times the capacity of MoO₂/C-G over all cycles. As expected, the size reduction of the agglomerates by the post treatment and the associated surface enlargement leads to an increased electrochemical activity of MoO₂/C-G as electrolyte diffusion is facilitated [48]. The initial increase in capacity of the MoO₂/C-G samples may be attributed to a gradual decomposition of Li_xMoO₂ in the conversion reaction during cycling [43], the formation of crystalline defects which is a common phenomenon in oxide anodes resulting in increasing capacity [49][50*], and/or a reaction including the SEI [50]. The rate capability of MoO₂/C-G(M) at cycle rates between

100 and 1000 mA g⁻¹ displayed in Fig. 7b implies a reversible capacity of 740, 580, 400, and 210 mA h g⁻¹, at a current density of 100, 250, 50 and 1000 mA g⁻¹, respectively. The reversible capacitance reaches 650 mA h g⁻¹ when the current density is set again to 100 mA g⁻¹, which proves good reversibility of the electrode. To characterize the microstructure details of the MoO₂/C-G(M) based electrode before and after galvanostatic cycling, *ex-situ* SEM measurements were performed (Fig. S4). The comparison of the SEM images before (Fig. S4a) and after (Fig. S4b) cycling reveals that the individual particles change their surface texture, which is likely due to the known degeneration mechanisms such as SEI formation [51] and/or agglomeration. Pulverization as a possible degeneration phenomenon for MoO₂/C-G(M) seems to be less critical as the high-resolution SEM images show that even after 60 cycles the binder network is intact and no clear cracks are visible.

To relate the electrochemical performance of the here presented MoO₂/C-G(M) composite to the literature, Table 2 lists the discharge capacities of various MoO₂/C composite anodes. The MoO₂/C-G(M)-based electrode studied at hand exhibits a superior electrochemical capacity compared to the materials obtained by Che *et al.* [21], Yoon *et al.* [52] and Luo *et al.* [40] and is slightly better than the materials reported by Sun *et al.* [53] and Hu *et al.* [54]. However, MoO₂/graphene oxide composite materials generally show higher capacities [16,41,55]. In contrast to these materials, the MoO₂/C-G(M) composite reported here benefits from a straightforward, environment-friendly, and well-controllable synthesis process, which is based on cost-effective starting materials. Evidently, the electrochemical performance of MoO₂/C composites mainly depends on morphological features as carbon coating, particle size and surface texture which are directly affecting the transport path length of electrons as well as Li-ions.

Table 2. Comparison of the electrochemical cycling performance of MoO₂-based composites obtained by various synthesis methods.

Material	Synthesis method	Current (mA g ⁻¹)	Discharge capacity (mAh g ⁻¹)/cycle no [*]	Ref.
MoO ₂ /C-G(M) nanoparticles	Glucose-assisted sol- gel	100	660/10	this work
MoO ₂ /C nanoparticles	Alginate-assisted sol-gel	200	300/10	[21]
Nitrided MoO ₂	hydrothermal	120	310/10	[52]
MoO ₂ /C nanofibers	Electrospinning	100	500/10	[40]
MoO ₂ /C nanoparticles	Impregnation of carbon matrix	100	600/10	[53]
MoO ₂ /graphite oxide nanoparticles	Solvothermal	100	620/10	[54]
MoO ₂ /graphite oxide nanoparticles	Solvothermal	100	800/10	[16]
MoO ₂ /C cage-like particle	Hydrothermal reduction	200	800/10	[22]
MoO ₂ /exfoliated graphene oxide	Solid-state graphenothermal reduction	100	850/10	[55]
MoO ₂ /graphene oxide	Decomposition	100	1200/10	[41]

*For better comparison, data from the same cycle number are shown as read-off from reported figures.

Conclusions

In summary, a tartaric acid and glucose based sol-gel method combined with thermal reduction has been utilized to synthesize hybrid MoO₂/C nanocomposites. This synthetic strategy is simple, cost-effective, and promising for large-scale industrial production of MoO₂/C composites. In the as-prepared composites, MoO₂ nanoparticles with a size of about 20 nm are embedded into a ~10 nm thick amorphous carbon matrix, which serves as a buffer layer preventing the degradation of MoO₂ nanoparticles during charge/discharge processes.

The observed electrochemical performances of the prepared materials underline the relevance of the used carbon source and the received morphology for the application in LIB. Compared to untreated MoO₂/C-G, post treated MoO₂/C-G(M) shows a clearly improved capacity. The post treated MoO₂/C-G(M) features a remarkably enhanced, competitive specific capacity of 660 mAh g⁻¹ at 100 mA g⁻¹ in the tenth cycle. Therefore, the results show that this simple and cost-effective synthesis approach may also be successfully applied to other metal oxides.

Acknowledgements

This work was supported by the Deutsche Forschungsgemeinschaft through projects KL 1824/12-1 and KL 1824/14-1. G.Z. acknowledges support of the state order via the Ministry of Science and High Education of Russia (Theme no. AAAA-A19-119031890025-9). Partial support by the BMWi through project 03ET6095C (HiKoMat) is acknowledged. The authors thank I. Glass for experimental support.

References

- [1] T. Yunusi, C. Yang, W. Cai, F. Xiao, J. Wang, X. Su, Synthesis of MoO₃ submicron belts and MoO₂ submicron spheres via polyethylene glycol-assisted hydrothermal method and their gas sensing properties, *Ceramics International* 39 (2013) 3435–3439.
- [2] A. Bento, A. Sanches, E. Medina, C.D. Nunes, P.D. Vaz, MoO₂ nanoparticles as highly efficient olefin epoxidation catalysts, *Appl. Catalysis A* 504 (2015) 399-407.
- [3] J. Liu, Z. Zhang, C. Pan, Y. Zhao, X. Su, Y. Zhou, D. Yu, Enhanced field emission properties of MoO₂ nanorods with controllable shape and orientation, *Mater. Lett.* 58 (2004) 3812-3815.
- [4] S.T. Nishanthi, A. Baruah, K.K. Yadav, D. Sarker, S. Ghosh, A.K. Ganguli, M. Jha, New low temperature environmental friendly process for the synthesis of tetragonal MoO₂ and its field emission properties, *Appl. Surface Sci.* 467-468 (2019) 1148-1156.
- [5] L. Li, H. Sui, K. Zhao, W. Zhang, X. Li, S. Liu, K. Yang, M. Wu, Y. Zhang, Preparation of carbon nanofibers supported MoO₂ composites electrode materials for application in dye-sensitized solar cells, *Electrochim. Acta* 259 (2018) 188-195.
- [6] G. Xu, P. Liu, Y. Ren, X. Huang, Z. Peng, Y. Tang, H. Wang, Three-dimensional MoO₂ nanotextiles assembled from elongated nanowires as advanced anode for Li ion batteries, *J. Power Sources* 361 (2017) 1–8.
- [7] Q. Xie, X. Zheng, D. Wu, X. Chen, J. Shi, X. Han, X. Zhang, G. Peng, Y. Gao, H. Huang, High electrical conductivity of individual epitaxially grown MoO₂ nanorods, *Appl. Phys. Lett.* 111 (2017) 093505.
- [8] L.C. Yang, Q.S. Gao, Y. Tang, Y.P. Wu, R. Holze, MoO₂ synthesized by reduction of MoO₃ with ethanol vapor as an anode material with good rate capability for the lithium ion battery, *J. Power Sources* 179 (2008) 357–360.

- [9] Y. Liang, Z. Yi, S. Yang, L. Zhou, J. Sun, Y. Zhou, Hydrothermal synthesis and lithium-intercalation properties of MoO₂ nano-particles with different morphologies, *Solid State Ionics* 177 (2006) 501–505.
- [10] Huanhuan Sun, Yu Zhang, Huanyan Liu, Xingyuan Zhang, Jian-Gan Wang, Constructing hierarchical MoO₂/N-doped carbon hydrangea-like spheres with superior lithium storage properties; *Journal of Alloys and Compounds* 787 (2019) 45-52.
- [11] L. Zhang, W. He, M. Ling, K. Shen, Y. Liu, S. Guo, Cu@MoO₂@C nanocomposite with stable yolk-shell structure for high performance lithium-ion batteries, *Journal of Alloys and Compounds* 768 (2018) 714–721.
- [12] X. Li, Q. Xiao, Y. Gao, H. Zhang, H. Xu, Y. Zhang, Hierarchical MoO₂/C microspheres: Preparation and application as anode materials for lithium ion batteries, *Journal of Alloys and Compounds* 723 (2017) 1113–1120.
- [13] P. Zhang, L. Zou, H. Hu, M. Wang, J. Fang, Y. Lai, J. Li, 3D Hierarchical carbon microflowers decorated with MoO₂ nanoparticles for lithium ion batteries, *Electrochim. Acta* 250 (2017) 219–227.
- [14] Xingyuan Zhanga, Jian-Gan Wanga, Wei Huaa, Hongzhen Liua, Bingqing Weiaa; Hierarchical nanocomposite of hollow carbon spheres encapsulating nano-MoO₂ for high-rate and durable Li-ion storage; *Journal of Alloys and Compounds* 787 (2019) 301-308.
- [15] K.H. Seng, G.D. Du, L. Li, Z.X. Chen, H.K. Liu, Z.P. Guo, Facile synthesis of graphene–molybdenum dioxide and its lithium storage properties, *J. Mater. Chem.* 22 (2012) 16072–16077.
- [16] Y. Xu, R. Yi, B. Yuan, X. Wu, M. Dunwell, Q. Lin, L. Fei, S. Deng, P. Andersen, D. Wang, H. Luo, High capacity MoO₂/graphite oxide composite anode for lithium-ion batteries, *J. Phys. Chem. Lett.* 3 (2012) 309–314.

- [17] Q. Gao, L. Yang, X. Lu, J. Mao, Y. Zhang, Y. Wu, Y. Tang, Synthesis, characterization and lithium-storage performance of MoO₂/carbon hybrid nanowires, *J. Mater. Chem.* 20 (2010) 2807–2812.
- [18] Y. Qi, B. Zhou, X. Yang, Y. Zhou, W. Jin, J. Zhou, W. Chen, 3D microstructures with MoO₂ nanocrystallines embedded into interpenetrated carbon nanosheets for lithium ion batteries, *J. Mater. Sci.: Mater. Electronics* 29 (2018) 11521–11528.
- [19] P. Zhang, L. Zou, H. Hu, M. Wang, J. Fang, Y. Lai, J. Li, 3D hierarchical carbon microflowers decorated with MoO₂ nanoparticles for lithium ion batteries, *Electrochim. Acta* 250 (2017) 219–227.
- [20] X. Li, Q. Xiao, Y. Gao, H. Zhang, H. Xu, Y. Zhang, Hierarchical MoO₂/C microspheres: Preparation and application as anode materials for lithium ion batteries, *Journal of Alloys and Compounds* 723 (2017) 1113–1120.
- [21] Y. Che, X. Zhu, J. Li, J. Sun, Y. Liu, C. Jin, C. Dong, Simple synthesis of MoO₂/carbon aerogel anodes for high performance lithium ion batteries from seaweed biomass, *RSC Adv.* 6 (2016) 106230–106236.
- [22] B. Liu, X. Zhao, Y. Tian, D. Zhao, C. Hu, M. Cao, A simple reduction process to synthesize MoO₂/C composites with cage-like structure for high performance lithium-ion batteries, *Phys. Chem. Chem. Phys.* 15 (2013) 8831–8837.
- [23] J. Ni, Y. Zhao, L. Li, L. Mai, Ultrathin MoO₂ nanosheets for superior lithium storage, *Nano Energy* 11 (2015) 129–135.
- [24] W. Cho, J.H. Song, J. Kim, G. Jeong, E.Y. Lee, Y. Kim, Electrochemical characteristics of nano-sized MoO₂/C composite anode materials for lithium-ion batteries, *J. Appl. Electrochem.* 42 (2012) 909–915.
- [25] J. Jiang, W. Yang, H.ao Wang, Y. Zhao, J. Guo, J. Zhao, M. Beidaghi, L. Gao, Electrochemical performances of MoO₂/C nanocomposite for sodium ion storage: an insight into rate dependent charge/discharge mechanism, *Electrochim. Acta* 240 (2017) 379–387.

- [26] K. Palanisamy, Y. Kim, H. Kim, J.M. Kim, W. Yoon, Self-assembled porous MoO₂/graphene microspheres towards high performance anodes for lithium ion batteries, *J. Power Sources* 275 (2015) 351–361.
- [27] L. Guo, Y. Wang, Standing carbon-coated molybdenum dioxide nanosheets on graphene: morphology evolution and lithium ion storage properties, *J. Mater. Chem. A* 3 (2015) 4706–4715.
- [28] J. Xiang, Z. Wu, X. Zhang, S. Yao, Enhanced electrochemical performance of an electrospun carbon/MoO₂ composite nanofiber membrane as self-standing anodes for lithium-ion batteries, *Mater. Res. Bull.* 100 (2018) 254–258.
- [29] A. Ottmann, G.S. Zakharova, B. Ehrstein, R. Klingeler, Electrochemical performance of single crystal belt-like NH₄V₃O₈ as cathode material for lithium-ion batteries, *Electrochim Acta* 174 (2015) 682–687.
- [30] A.L. Patterson, The Scherrer formula for X-Ray particle size determination. *Phys. Rev. Lett.* 56 (1939) 978–982.
- [31] V. Wang, D.C. Alsmeyer, R. L. McCreery, Raman spectroscopy of carbon materials: structural basis of observed spectra, *Chem. Mater.* 2 (1990) 557–563.
- [32] L. Kumari, Y.-R. Ma, C.-C. Tsai, Y.-W. Lin, S.Y. Wu, K.-W. Cheng, Y. Liou, X-ray diffraction and Raman scattering studies on large-area array and nanobranched structure of 1D MoO₂ nanorods, *Nanotechnology* 18 (2007) 115717.
- [33] G.S. Zakharova, Ch. Schmidt, A. Ottmann, E. Mijowska, R. Klingeler, Microwave-assisted hydrothermal synthesis and electrochemical studies of α - and h -MoO₃, *J. Solid State Electrochem.* 22 (2018) 3651–3661.
- [34] M.A. Camacho-Lopez, L. Escobar-Alarcyn, M. Picquart, R. Arroyo, G. Cyrdoba, E. Haro-Poniatowski, Micro-Raman study of the m -MoO₂ to α -MoO₃ transformation induced by cw-laser irradiation, *Optical Mater.* 33 (2011) 480–484.

- [35] X. Wang, Y. Liu, J. Zeng, C. Peng, R. Wang, MoO₂/C hollow nanospheres synthesized by solvothermal method as anode material for lithium-ion batteries, *Ionics* 25 (2019) 437–445.
- [36] F.O. Libnau, A.A. Christy, O.M. Kvalheim, Resolution of infrared spectra and kinetic analysis of mutarotation of D-glucose in water by sequential rank analysis, *Vibrational Spectroscopy* 7 (1994) 139-148.
- [37] N. Chumha, S. Kittiwachana, T. Thongtem, S. Thongtem, S. Kaowphong, Synthesis and characterization of GdVO₄ nanostructures by a tartaric acid-assisted sol–gel method, *Ceramics International* 40 (2014)16337–16342.
- [38] L. Yang, X. Li, Y. Ouyang, Q. Gao, L. Ouyang, R. Hu, J. Liu, M. Zhu, Hierarchical MoO₂/Mo₂C/C Hybrid nanowires as high-rate and long-life anodes for lithium-ion batteries, *ACS Appl. Mater. Interfaces* 8 (2016) 19987–19993.
- [39] J. Dahn, W. Mckinnon, Structure and electrochemistry of Li_xMoO₂, *Solid State Ionics*, 23 (1987) 1–7.
- [40] W. Luo, X. Hu, Y. Sun and Y. Huang, Electrospinning of carbon-coated MoO₂ nanofibers with enhanced lithium-storage properties, *Phys. Chem. Chem. Phys.* 13 (2011) 16735–16740.
- [41] Z. Xu, K. Yao, H. Fu, X. Shen, X. Duan, L. Cao, J. Huang, H. Wang, Constructing MoO₂ porous architectures using graphene oxide flexible supports for lithium ion battery anodes, *Global Challenges* 1 (2017) 1700050.
- [42] L. Zhou, H. Wu, Z. Wang, X. Lou, Interconnected MoO₂ nanocrystals with carbon nanocoating as high-capacity anode materials for lithium-ion batteries, *ACS Appl. Mater. Interfaces* 3 (2011) 4853–4857.
- [43] B. Guo, X. Fang, B. Li, Y. Shi, C. Ouyang, Y. Hu, Z. Wang, G. Stucky, L. Chen, Synthesis and lithium storage mechanism of ultrafine MoO₂ nanorods, *Chem. Mater.* 24 (2012) 457–463.
- [44] Y. Sun, X. Hu, W. Luo, and Y. Huang, Self-assembled hierarchical MoO₂/graphene nanoarchitectures and their application as a high-

- performance anode material for lithium-ion batteries, *ACS Nano* 5 (2011) 7100-7107.
- [45] J. Li, S. Hwang, F. Guo, S. Li, Z. Chen, R. Kou, K. Sun, C. Sun, H. Gan, A. Yu, E. Stach, H. Zhou, D. Su, Phase evolution of conversion-type electrode for lithium ion batteries, *Nature Commun.* 10 (2019) 2224.
- [46] M. Ebner, F. Marone, M. Stampanoni, V. Wood, Visualization and quantification of electrochemical and mechanical degradation in Li ion batteries, *Science* 342 (2013) 716-720.
- [47] A. Ottmann, M. Scholz, E. Thae, P. Schneider, M. Gellesch, C. Nowka, S. Wurmehl, S. Hampel, R. Klingeler, Electrochemical magnetization switching and energy storage in manganese oxide filled carbon nanotubes, *Sci. Rep.* 7 (2017) 13625.
- [48] C. Delacourt, P. Poizot, S. Levasseur, C. Masquelier, Size effects on carbon-free LiFePO_4 powders: The key to superior energy density, *Electrochem. Solid State Lett.* 9 (2006) A352-A355.
- [49] Kun Chang, Dongsheng Geng, Xifei Li, Jinli Yang, Yongji Tang, Mei Cai, Ruying Li, and Xueliang Sun, Ultrathin MoS_2 /Nitrogen-Doped Graphene Nanosheets with Highly Reversible Lithium Storage, *Adv. Energy Mater.* 2013, 3, 839–844
- [50] Yan-Yan Hu¹, Zigeng Liu, Kyung-Wan Nam, Olaf J. Borkiewicz, Jun Cheng, Xiao Hua¹, Matthew T. Dunstan, Xiqian Yu, Kamila M. Wiaderek, Lin-Shu Du, Karena W. Chapman, Peter J. Chupas, Xiao-Qing Yang² and Clare P. Grey, Origin of additional capacities in metal oxide lithium-ion battery electrodes, *Nature Materials*, vol 12, 2013.
- [51] Fanyan Zeng, Maohui Yu, Wanting Cheng, Wenxiu He, Yang Pan, Yaohui Qu, and Cailei Yuan, Tunable Surface Selenization on MoO_2 -Based Carbon Substrate for Notably Enhanced Sodium-Ion Storage Properties, *Small* 2020, 2001905

- [52] Sukeun Yoon, Kyu-Nam Jung, Chang Soo Jin, Kyung-Hee Shin; Synthesis of nitrated MoO₂ and its application as anode materials for lithium-ion batteries; *Journal of Alloys and Compounds* 536 (2012) 179–183
- [53] Y. Sun, X. Hu, W. Luo, Y. Huang, Ultrafine MoO₂ nanoparticles embedded in a carbon matrix as a high-capacity and long-life anode for lithium-ion batteries, *J. Mater. Chem.* 22 (2012) 425–431.
- [54] S. Hu, F. Yin, E. Uchaker, W. Chen, M. Zhang, J. Zhou, Y. Qi, G. Cao, Facile and green preparation for the formation of MoO₂-GO composites as anode material for lithium-ion batteries, *J. Phys. Chem. C* 118 (2014) 24890–24897.
- [55] S. Petnikota, K.W. Teo, L. Chen, A. Sim, S.K. Marka, M.V. Reddy, V.V.S.S. Srikanth, S. Adams, B.V.R. Chowdari, Exfoliated graphene oxide/MoO₂; Composites as anode materials in lithium-ion batteries: An insight into intercalation of Li and conversion mechanism of MoO₂, *ACS Appl. Mater. Interfaces* 8 (2016) 10884–10896.